Knudsen-number dependence of two-dimensional single-mode Rayleigh-Taylor fluid instabilities

Irina Sagert,[1] Jim Howell,[2] Alec Staber,[2] Terrance Strother,[3] Dirk Colbry,[2] and Wolfgang Bauer[2,4]
[1]*Center for Exploration of Energy and Matter, Indiana University, Bloomington, Indiana 47308, USA*
[2]*Institute for Cyber-Enabled Research, Michigan State University East Lansing, Michigan 48824, USA*
[3]*XTD-IDA, Los Alamos National Laboratory, Los Alamos, New Mexico 87545, USA*
[4]*Department of Physics and Astronomy, Michigan State University, East Lansing, Michigan 48824, USA*
(Received 23 October 2014; revised manuscript received 11 May 2015; published 8 July 2015)

We present a study of single-mode Rayleigh-Taylor instabilities with a modified direct simulation Monte Carlo (MDSMC) code in two dimensions. The MDSMC code is aimed to capture the dynamics of matter for a large range of Knudsen numbers within one approach. Our method combines the traditional Monte Carlo technique to efficiently propagate particles and the point-of-closest-approach method for high spatial resolution. Simulations are performed using different particle mean free paths and we compare the results to linear theory predictions for the growth rate including diffusion and viscosity. We find good agreement between theoretical predictions and simulations and, at late times, observe the development of secondary instabilities, similar to hydrodynamic simulations and experiments. Large mean free paths favor particle diffusion, reduce the occurrence of secondary instabilities, and approach the noninteracting gas limit.

DOI: 10.1103/PhysRevE.92.013009 PACS number(s): 47.20.−k, 47.11.−j, 07.05.Tp, 47.45.−n

I. INTRODUCTION

Dynamical simulations that are based on interacting particles are increasingly applied in different physical fields. Different from conventional hydrodynamics methods that operate in the continuum limit, kinetic approaches are able to simulate matter at all Knudsen numbers $K = l/L$. Here l is the particle mean free path and L is a characteristic length scale. Examples of research areas that apply kinetic methods include material science [1,2], nuclear collisions [3–9], and plasma physics [10–12]. In astrophysics, particle methods have a long history in radiation transport [13–19] and cosmological simulations [20]. Modern usage also includes nuclear matter in neutron star crusts [21] and neutrino transport in core-collapse supernovas (CCSNs) [22,23]. Furthermore, particle methods have received a large amount of interest from studies of inertial confinement fusion (ICF) capsule implosion performed at the National Ignition Facility [10–12,24–27].

Advantages of kinetic methods include their flexibility with regard to optical depths, the facility to include complex geometries and distributions of matter, and the correct representation of the Boltzmann transport of many particles in three dimensions. A current drawback in comparison to hydrodynamic simulations of macroscopic systems is the large number of particles that is required to accurately represent a physical problem and reduce statistical noise. For example, large optical depths require many particle interactions and the corresponding simulations become increasingly slow. However, as computational power increases, the relatively straightforward parallelization and scalability of particle codes [28–30] could outweigh the computational costs.

Depending on the physical problem, different particle-based simulation techniques are used. Some more widely used approaches simulations include molecular dynamics [31,32], direct simulation Monte Carlo [33–35], and particle in cell [36,37]. While all approaches have been primarily developed to describe nonequilibrium matter, they are able to retrieve macroscopic variables such as density, fluid velocity, pressure, and temperature. Furthermore, they can model the evolution of hydrodynamic phenomena such as shock waves [38–44] and fluid instabilities [45–53]. Both are important components in plasma and astrophysics.

Our goal is to develop a large-scale kinetic transport code that can handle more than 10^6 particles in a computationally efficient way and thereby simulate matter in nonequilibrium and in the hydrodynamic regime. With that, we want to study astrophysical phenomena such as CCSNs [54,55]. Furthermore, this approach could be applied in the simulation of ICF capsule dynamics [24–27]. The evolution of both systems, CCSNs and ICF, is largely governed by shock wave dynamics paired with fluid instabilities and nonequilibrium particle transport [55–63].

Our modified direct simulation Monte Carlo (MDSMC) code has already been successfully tested on shock wave phenomena in nonequilibrium and in the continuum regime [39,64]. In this work we present a detailed study of fluid instabilities in two dimensions. Here we focus on the single-mode Rayleigh-Taylor instability (SMRTI) [65]. Our motivation is the possible important role of RTIs in ICF and CCSN dynamics. The advantage of the SMRTI is that at early stages, it can be compared to an analytic solution from linear theory. With that, we can refer to the latter and experiments for comparison. Fluid instability simulations including RTIs have been performed by particle codes in the past (see, e.g., [45,66]). In this paper we present a detailed and comprehensive analysis for a large range of particle mean free paths.

In the following we give a short introduction of RTIs in Sec. II, followed by an overview of our MDSMC code in Sec. III. We then proceed with our simulation setup and discuss the results for varying particle mean free paths in Secs. IV and V. The paper closes with a summary and outlook in Sec. VI.

II. RAYLEIGH-TAYLOR INSTABILITIES

Rayleigh-Taylor instabilities form at the interface of two fluids with different densities when the less dense fluid is pushing against the one with higher density. A typical example

is a heavy fluid resting on top of a lighter one in the presence of a gravitational acceleration [67,68]. In such a case, small perturbations at the fluid interface grow and result in the development of RTIs. The latter can be found in many different physical environments, ranging from astrophysical systems to geophysical phenomena. Due to their large dynamical impact and the direct connection with turbulent mixing, RTIs receive a great deal of interest. Studies have been performed analytically, experimentally, and numerically [69–71], while the growing computational power allows one to study RTI phenomena in greater detail and for increasingly larger systems.

In realistic environments, fluid instabilities of many different wave numbers can be present. For code validation studies, it is easier to focus on the SMRTI that arises from an initial perturbation $\eta_0(x)$ with a defined wavelength λ. Its evolution can be divided into several major stages.

During the first stage, the amplitude of the initial perturbation is $2B \lesssim 0.5\lambda$. Here the instability undergoes exponential growth, which can be described by linear analysis [72,73]

$$\eta(x,t) = 0.5(e^{\gamma t} + e^{-\gamma t})\eta_0(x). \tag{1}$$

For ideal fluids, the growth rate γ is given by

$$\gamma = \sqrt{Agk}, \quad A = \frac{\rho_2 - \rho_1}{\rho_2 + \rho_1}, \quad k = 2\pi/\lambda, \tag{2}$$

A being the Atwood number and k the wave number. The densities of the light and heavy fluids are given by ρ_1 and ρ_2, respectively. When diffusion and viscosity are included, the growth rate changes to

$$\gamma(t) = \sqrt{\frac{Agk}{\phi(A,t)} + \nu^2 k^4} - (\nu + \xi)k^2. \tag{3}$$

Here $\phi(A,t)$ represents dynamic diffusion effects, ξ is the diffusion coefficient, and ν is the kinematic viscosity. Note that, different from the ideal fluid approximation in Eq. (2), the viscous growth rate is dependent on time t.

When $B > \lambda$, nonlinear effects start to dominate. Light fluid bubbles rise into the denser phase, while spikes of the latter sink downward. Perturbations with large wave numbers are generated and aerodynamical deceleration of sinking spikes leads to the formation of mushroom-shaped jets [74]. As bubbles and spikes start to interact with each other, the dynamics become chaotic, leading to turbulent mixing.

The effects that compressibility, viscosity, and surface tension have on the evolution of the RTI have been discussed in, e.g., [75,76]. Here surface tension and viscosity are found to stabilize perturbations while simulations using compressible fluids experience delays in the formation of the mushroom-shaped jets. Challenges in numerical studies of RTIs arise in the nonlinear regime when a finer computational grid leads to the development of more secondary instabilities. This is partly due to the finer resolution and partly due to the use of a different grid. Convergence tests are generally performed to ensure that the dynamics of the simulated system do not change with resolution.

III. MODIFIED DSMC APPROACH

Here we present a short overview of our simulation method adjusted to two-dimensional (2D) calculations. A general discussion can be found in [39]. The foundation of our approach is a DSMC method where the phase space of the physical problem is represented by N δ functions or so-called test particles:

$$f(\mathbf{r},\mathbf{p},t) = \sum_{i=0}^{N} \delta^2(\mathbf{r} - \mathbf{r}_i(t))\delta^2(\mathbf{p} - \mathbf{p}_i(t)). \tag{4}$$

Here $\mathbf{r}_i$ is the position and $\mathbf{p}_i$ the momentum of the ith test particle. This distribution function is used as input into the Boltzmann equation [77] and results in $2N$ ordinary differential equations of motion for each test-particle with mass m_i:

$$\frac{d}{dt}\mathbf{p}_i = \mathbf{F}(\mathbf{r}_i) + \mathcal{C}(\mathbf{p}_i), \tag{5}$$

$$\frac{d}{dt}\mathbf{r}_i = \frac{\mathbf{p}_i}{m_i}, \quad i = 1,\ldots,N. \tag{6}$$

Particles interact with each other via one-body mean-field forces $\mathbf{F}(\mathbf{r}_i)$, such as gravity. In addition, they undergo two-body interactions, which are symbolized by $\mathcal{C}(\mathbf{p}_i)$. For realistic fluids, the latter must contain the appropriate cross section σ. In the current study, we want to test the continuum behavior of our code. Particle interactions are therefore modeled as simple elastic collisions. The implementation of more complex interactions, as has already been done in previous works for CCSN simulations [78–80], is beyond the scope of the present paper. For elastic collisions, the 2D cross sections are related to a particle effective interaction radius $\sigma_{2D} = 2_{\text{eff}}$. Here r_{eff} is determined by the particle mean free path l and the number density n, which is defined as the number of particles N divided by the area A:

$$r_{\text{eff}} = 1/2ln, \quad n = N/A. \tag{7}$$

As in our previous works, l will be used as an input variable. From that, we determine the particle effective radii and apply them in our collision partner search [39]. Hereby, we calculate the time t_o at which the effective radii of both particles overlap:

$$t_{o(1,2)} = t_p \pm \sqrt{t_p^2 - t_{\text{rel}}^2 + t_{\text{eff}}^2}, \tag{8}$$

$$t_p = -(\mathbf{r}_{\text{rel}} \cdot \mathbf{v}_{\text{rel}})/|\mathbf{v}_{\text{rel}}|^2, \tag{9}$$

$$t_{\text{rel}} = |\mathbf{r}_{\text{rel}}|/|\mathbf{v}_{\text{rel}}|, \tag{10}$$

$$t_{\text{eff}} = (r_{\text{eff},A} + r_{\text{eff},B})/|\mathbf{v}_{\text{rel}}|. \tag{11}$$

If either t_{o1} or t_{o2} is a real number, a collision can take place [39]. Otherwise, the particles are too far away from each other. Note that the effective radii are utilized in this step only. For the actual interaction time we choose the point-of-closest-approach (POCA) method, which is different from the usual DSMC routine. Here the collision is performed at t_p, when two particles reach their minimal distance. With that, the POCA algorithm reduces causality violations, which are often present in DSMC-type simulations [9]. The combination of DSMC and POCA results in a favorable scaling of the computational time with N [39,81] and an improved spatial accuracy. When the collision is performed at the point of closest approach, the

outgoing particle velocity vectors are determined randomly in the center-of-mass (c.m.) frame of the colliding pair

$$\phi = 2\pi\kappa, \quad \kappa \in [0.0, 1.0], \tag{12}$$

$$v_{x,\text{out,c.m.}} = v_{\text{in,c.m.}} \cos(\phi), \tag{13}$$

$$v_{y,\text{out,c.m.}} = v_{\text{in,c.m.}} \sin(\phi), \tag{14}$$

$$v_{\text{in,c.m.}} = \sqrt{v^2_{x,\text{in,c.m.}} + v^2_{y,\text{in,c.m.}}}. \tag{15}$$

From the c.m. frame they are then transformed back into the laboratory frame.

At the beginning of each time step, particles are sorted into their spatial cells or bins where they can only interact with partners in their own bin or adjacent cells. To prevent particles from traveling beyond their collision neighborhood during a time step Δt, the latter is given by the cell size Δx divided by the maximum particle velocity:

$$\Delta t(t) = \Delta x / v_{\max(t)}. \tag{16}$$

We use Euler's method to iterate the equations of motion

$$\mathbf{r_i}(t + \Delta t) = \mathbf{r_i}(t) + \mathbf{v}_{\text{old},i} t_p + \mathbf{v}_{\text{new},i}(\Delta t - t_p), \tag{17}$$

$$\mathbf{r_i}(t + \Delta t) = \mathbf{r_i}(t) + \mathbf{v}_{\text{old},i} \Delta t, \tag{18}$$

where Eq. (17) is applied when a collision takes place and Eq. (18) otherwise. Computationally expensive sorting algorithms are not necessary as we represent each grid cell via a linked list of particles it contains, which only requires a simple coordinate check.

Our code can perform simulations in two and three dimensions, whereas the degrees of freedom and matter equation of state change accordingly. The collision partner search is parallelized using shared memory parallelization via OpenMP. However, our 2D RTI studies are long-time simulations. Using OpenMP with 32 processors, they take on average $\sim 1.2 \times 10^5$ time steps in $\sim$350 h. To enable larger 2D and 3D simulations in the future, a distributed memory parallelization via the message-passage interface (MPI) is necessary and is currently under development [81]. The scaling of the collision partner search has been tested in the current OpenMP and preliminary MPI setups and is close to ideal for 2D and 3D simulations [39,81]. In general, our study of the SMRTI uses the same algorithm as in [39], however, we include a change in the boundary conditions for the long-time evolution of the RTI (see the next section).

IV. SIMULATION SETUP

A. Particle initialization

The 2D SMRTI is initialized as a heavy fluid with density ρ_2 lying on top of a light one with $\rho_1 = 0.5\rho_2$. The box size is $0 \leqslant x \leqslant L_x$ and $0 \leqslant y \leqslant L_y$. Both fluids are initially at rest with a pressure P_0 at the fluid interface. The units of all quantities are given by the dimensions of length $\tilde{L}$, density $\tilde{\rho}$, and pressure $\tilde{P}$. Consequently, the units for velocity are $\sqrt{\tilde{P}/\tilde{\rho}}$, the units for time $\tilde{L}\sqrt{\tilde{\rho}/\tilde{P}}$, and the units for the gravitational acceleration $\tilde{P}/\tilde{L}\tilde{\rho}$. In the latter, g is set to 1.0 and is pointing in the negative-y direction. The simulation space is divided into two equally sized areas $A_1 = A_2$, where A_2 contains the high-density fluid while the low-density fluid is in A_1. Both subspaces contain the same number of test particles $N_1 = N_2$ with masses $m_{1,2} = \rho_{1,2} A_{1,2}/N_{1,2}$. To keep track of their motion, particles in A_2 are assigned a particle type $\tau_2 = 2$, while particles A_1 are given $\tau_1 = 1$.

The pressure as a function of the y position is given by the barometric formula. Assuming that the densities ρ_1 and ρ_2 are constant and do not depend on the height, the expression for the pressure is given by

$$P_{1,2}(y) = P_0 + \rho_{1,2} g (y - 0.5 L_y), \tag{19}$$

where we choose $P_0 = 2.5$. This allows the determination of the temperature at height y via the ideal gas law

$$kT_{1,2}(y) = P_{1,2}(y)/n_{1,2}. \tag{20}$$

With given P, $k\,T$, and their connection to the the root-mean-square velocity $P = v^2_{\text{rms}}\, nm/2$, we can initialize absolute velocities for each particle i at y_i with random directions by a 2D Maxwell-Boltzmann (MB) distribution

$$F_{2\text{D},v}(v, y_i) = \left(\frac{m}{2\pi k T(y_i)}\right) \exp\left(-\frac{m v^2}{k T(y_i)}\right) \tag{21}$$

and a Monte Carlo algorithm [82]. Furthermore, to initialize the SMRTI, a perturbation $\eta_0(x)$ is introduced via a modification to the fluid interface

$$\eta_0(x) = 0.5 L_y + B_0 \cos(2\pi x/\lambda) \tag{22}$$

with an amplitude $B_0 = 0.01$ and wavelength $\lambda = 2L_x$.

B. The RTI growth rate with D and ν

In 2D systems, expressions for the dynamic viscosity μ and diffusion coefficient ξ can be determined from kinetic theory (using the approach of [83])

$$\mu = \rho \bar{v} l/2, \quad \xi = \bar{v} l/2. \tag{23}$$

Here $\bar{v}$ is the 2D mean velocity

$$\bar{v} = \sqrt{kT/2m} \tag{24}$$

and the kinematic viscosity ν in Eq. (3) can be obtained by $\nu = \mu/\rho = \xi$. To determine $\phi(A,t)$ in Eq. (3), we apply the approach of [84] and numerically solve the following eigenvalue equation for the vertical velocity component ω:

$$a^2(t) \frac{d}{d\sigma}\left[\Psi \frac{d\omega}{d\sigma}\right] = \omega\left(\Psi - a(t)\phi \frac{dQ}{d\sigma}\right), \tag{25}$$

with

$$\Psi = 1 + AQ, \quad a(t) = 1/k\epsilon, \quad \epsilon = 2\sqrt{\xi t}, \tag{26}$$

$$Q(\sigma) = 2\pi^{-1/2} \int_0^\sigma \exp(-\zeta^2) d\zeta = \text{erf}(\zeta), \tag{27}$$

and σ being the scaled vertical direction $(y - 0.5L_y)/\epsilon$. The boundary conditions are $\omega \to 0$ for $\sigma \to \pm\infty$. For the solution, Eq. (25) is replaced by a finite-difference analogy. The value of $\omega(\sigma + \delta\sigma)$ can be obtained from the knowledge

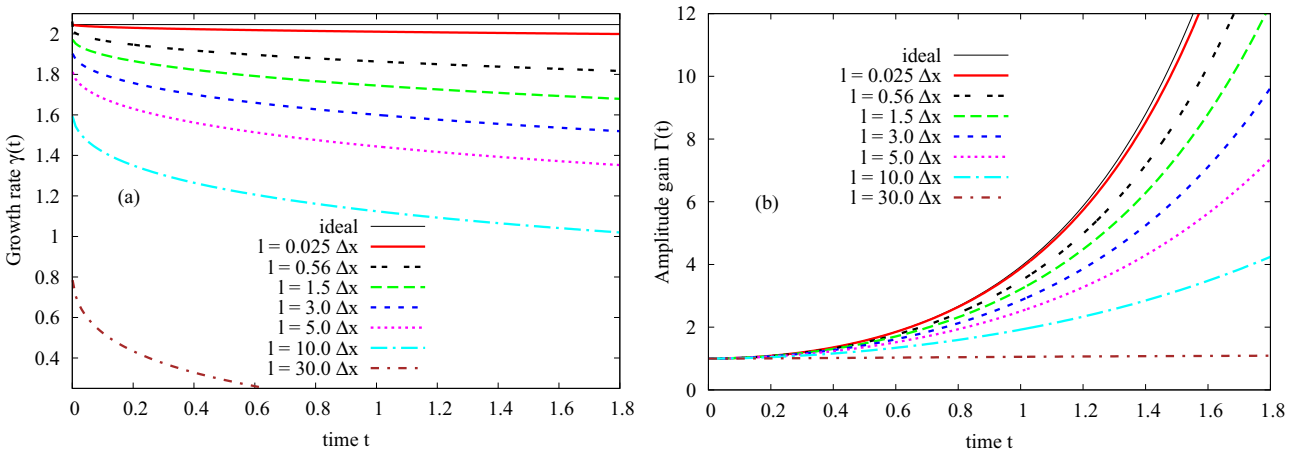

FIG. 1. (Color online) (a) Growth rate $\gamma(t)$ and (b) amplitude gain $\Gamma(t)$ for different mean free paths l according to Eqs. (3) and (29). The values of γ and Γ in the limit of ideal hydrodynamics are given by thin solid lines.

of $\omega(\sigma)$ and $d\omega(\sigma)/d\sigma$ via iterations. These are started at $\sigma \ll -1$, so $\omega(\sigma) = \exp(\sigma/a)$ can be assumed. For trial values of ϕ and assigned A and t, the solution for ω is obtained to sufficiently large σ. For the correct ϕ, ω should approach zero and otherwise diverge to $+\infty$ or $-\infty$. We apply a root-finding routine to determine the value of ϕ. Due to the time dependence of the growth rate $\gamma(t)$, the evolution of the instability is now given by

$$\eta(x,t) = \Gamma(t)\eta_0(x), \tag{28}$$

$$\Gamma(t) = 0.5(e^{\beta(t)} + e^{-\beta(t)}), \quad \beta(t) = \int_0^t \gamma(t)dt, \tag{29}$$

where $\beta(t)$ is determined by numerical integration. Figure 1 shows the values of $\gamma(t)$ and the amplitude gain $\Gamma(t)$ for $l = 0.025\Delta x - 100.0\Delta x$. The growth rate is almost constant for $l = 0.025\Delta x$ and close its ideal fluid value of $\gamma \sim 2.046$. For larger mean free paths, viscosity and diffusion lead to a decrease in $\gamma(t)$. For $l = 100.0\Delta x$, we find that $\gamma < 0$ at all times, which implies that the SMRTI evolution is dominated by diffusive effects from the very beginning [71,84]. In this case, an instability will not develop and the two gases will diffuse into each other. Table I lists the exact values of $\Gamma(t)$ for $t = 0.5$, 1.25, and 1.75 together with the kinematic viscosities ν, Reynolds numbers [71]

$$R = \lambda\nu^{-1}\sqrt{A(A+1)^{-1}g\lambda}, \tag{30}$$

and nondiffusive viscous growth rates $\gamma_{\rm nd}$ and $\Gamma_{\rm nd}$ [72]. The latter are similar to Γ but generally higher, which leads to a faster SMRTI evolution. For comparison with our simulations we will use the diffusive viscous growth rates $\Gamma(t)$.

C. Boundary conditions

Our previous studies apply simple reflective boundary conditions [39]. For example, if during Δt a particle with velocity $\mathbf{v}_{\rm old}$ crosses the box boundary at $y = b_y = 0$ to a position beyond the boundary $\mathbf{r}_{\rm old}$, its location and motion are updated via

$$x_{\rm new} = x_{\rm old}, \quad y_{\rm new} = -y_{\rm old}, \tag{31}$$

$$v_{{\rm new},x} = v_{{\rm old},x}, \quad v_{{\rm new},y} = -v_{{\rm old},y}. \tag{32}$$

For the current tests, we modify this simple approach.

In addition to the usual particle motion, we have to consider that the gravitational acceleration g is present at all times. When a particle is moving towards $b_y = 0$, it is accelerated downward. Once it is reflected by the wall and moves in the opposite direction, its y velocity is decreased due to g. Furthermore, with typically $O(10^5)$ simulation time steps, the sinusoidal form of the SMRTI instability together with the simple reflective boundary conditions could lead to the development of standing waves or shock waves in the simulation box. Since these could impact the evolution of the SMRTI, we modify the boundary conditions so that particles

TABLE I. Kinematic viscosities ν, amplitude gain with and without diffusion $\Gamma(t)$ (see the text) and $\Gamma_{\rm nd}(t)$ [72], respectively, growth rates without diffusion $\gamma_{\rm nd}$, and Reynolds numbers R for different particle mean free paths l.

l (Δx)	ν ($\sqrt{\tilde{P}/\tilde{\rho}}\,\tilde{L}$)	$\Gamma(t=0.5)$	$\Gamma(t=1.25)$	$\Gamma(t=1.75)$	$\gamma_{\rm nd}$	$\Gamma_{\rm nd}(t=1.75)$	R
0.025	3.515×10^{-6}	1.559	6.338	17.156	2.025	17.313	5.030×10^{5}
0.56	7.873×10^{-5}	1.515	5.457	13.548	1.934	14.769	2.245×10^{3}
1.5	2.109×10^{-4}	1.485	4.881	11.322	1.852	12.800	8.383×10^{2}
3.0	4.217×10^{-4}	1.426	4.172	8.931	1.759	10.883	4.192×10^{2}
5.0	7.029×10^{-4}	1.363	3.508	6.891	1.661	9.176	2.515×10^{2}
10.0	1.406×10^{-3}	1.244	2.456	4.040	1.471	6.599	1.257×10^{2}
30.0	4.217×10^{-3}	1.024	1.069	1.089	1.005	2.989	4.192×10^{1}

that interact with the walls receive a random new direction of motion. We refer to these as random reflective boundary conditions.

To implement these modification, we determine the particle-boundary collision time t_b from

$$b_y = y_{\text{old}} + v_{\text{old},y} t_b + g t_b^2/2, \tag{33}$$

$$t_b = \frac{1}{g}\left[-v_{\text{old},y} \pm \sqrt{v_{\text{old},y}^2 - 2(y_{\text{old},y} - b_y)}\right], \tag{34}$$

where $b_y = L_y$ or $b_y = 0$. The incoming y velocity at b_y is given by

$$v_{b,y} = v_{\text{old},y} + g t_b. \tag{35}$$

Together with the unchanged particle motion in the x direction, the absolute velocity v_b at b_y becomes

$$v_b = \sqrt{v_{b,y}^2 + v_{x,\text{old}}^2}. \tag{36}$$

To determine the postreflection velocity, the outgoing direction of motion is randomized. For that, we create random numbers $\kappa_x \in [-1.0,1.0]$ and $\kappa_y \in [0.0,1.0]$ or $\kappa_y \in [-1.0,0.0]$, depending on whether the reflection is performed at $b_y = 0$ or $b_y = L_y$, respectively. The random numbers are scaled so that $\kappa_x^2 + \kappa_y^2 = 1$ and the new velocity components and positions are calculated as

$$v_{\text{new},y} = v_b \kappa_y + g(\Delta t - t_b), \tag{37}$$

$$v_{\text{new},x} = v_b \kappa_x, \tag{38}$$

$$y_{\text{new},y} = b_y + v_b \kappa_y (\Delta t - t_b) + g(\Delta t - t_b)^2/2, \tag{39}$$

$$x_{\text{new},x} = x_{\text{old}} + v_{\text{old},x} t_b + v_{\text{new},x}(\Delta t - t_b). \tag{40}$$

With that, our simulation should be able to disperse incoming waves and shocks at the boundaries and thereby minimize wall effects.

D. Minimal mean free path

In our previous studies [39], we set the mean free path to small values of, e.g., $l = 10^{-3}\Delta x$ to simulate matter in the continuum regime. This was motivated by the effective particle radius being dependent not only on l but also on the particle number per bin $N = N_{\text{bin}}$ as is shown in Eq. (7) with $A = A_{\text{bin}} = (\Delta x)^2$. In our shock wave studies, N_{bin} varies up to a factor ∼50. In this case, setting l to a small value $l \ll \Delta x$ ensures that the effective radii stay sufficiently large for particles to see all potential interaction partners in the collision neighborhood. For the SMRTI, the number of particles per calculation bin fluctuates around $N_{\text{bin}} \sim 10$. Considering that a particle can only detect collision partners in its collision neighborhood, we can set a maximal limit on the effective radius to $r_{\text{eff,max}} \sim 2\Delta x$ (considering two interacting particles at opposite corners of the collision neighborhood), which results in a minimal value of the mean free path

$$l_{\text{min},1} = \Delta x/4N_{\text{bin}} \sim 0.025\Delta x. \tag{41}$$

Although for $l \ll l_{\text{min},1}$ the effective radii technically increase, particles are still unable to see beyond the collision neighborhood. While all simulations with $l \leqslant l_{\text{min},1}$ should therefore evolve similarly, comparisons with theoretical predictions that involve viscosity and diffusion should consider the true minimal value of l. As can be seen from Eq. (41), the only possibility to reduce $l_{\text{min},1}$ is to increase the value of N_{bin} keeping Δx constant, or decrease the latter at a constant N_{bin}. The value of l_{min} might even increase if we assume that in the continuum limit all particles interact and that collisions generally take place between close neighbors. In this case, we can determine r_{eff} from a particle area

$$A_p = \pi r_p^2 = A_{\text{bin}}/N_{\text{bin}}, \tag{42}$$

which implies

$$r_p = \sqrt{A_{\text{bin}}/\pi N_{\text{bin}}} = r_{\text{eff}}. \tag{43}$$

Again, in principle, a larger effective radius enables particles to see beyond their closest collision partner, however, the interaction will still take place between particles with a distance $\leqslant 2r_{\text{eff}}$. Using Eqs. (7) and (43) we arrive at a new mean-free-path limit of $l_{\text{min},2} = \sqrt{\pi/4N_{\text{bin}}}\Delta x \sim 0.28\Delta x$. Furthermore, in our collision algorithm, we discard interactions that involve more than two particles. This situation occurs frequently for close-to-continuum simulations and, as a result, about half of potential collisions are not performed when l is small [39]. To account for the fact that we have about 50% fewer collisions during a time step than anticipated and therefore more free streaming particles, we increase the minimal mean free path to

$$l_{\text{min},2} = 2{\times}0.28\Delta x = 0.56\Delta x. \tag{44}$$

In the following we will use $l = l_{\text{min},1}$ for our close-to-continuum simulations but also apply $l_{\text{min},2}$ when comparing results with theoretical predictions.

V. MEAN-FREE-PATH STUDIES

A. Evolution of a plane fluid interface

Before discussing the SMRTI simulations, we will study the evolution of a plane fluid interface with $B_0 = 0$. Different from hydrodynamic codes, the finite number of particles in kinetic methods always leads to small irregularities of the fluid interface. If not suppressed, these serve as the source for the development of large-scale instabilities. Figure 2 shows the evolution of the initially smooth interface for $t \leqslant 3.0$ using 10^7 test particles. The initialization of the simulation is as in Sec. IV, however the box size is chosen as $L_x = 0.8$ and $L_y = 0.5$ with $1280{\times}800$ calculation bins and $160{\times}100$ output bins. The boundary conditions are random reflective and particles are interacting with each other via simple elastic collisions according to the POCA algorithm using $l = l_{\text{min},1}$.

It can be seen from Fig. 2 that the seemingly smooth fluid interface develops a diffusion layer with small dips and peaks within $t \ll 1.0$. This mixing is due to the finite value of l that allows particles to move from one fluid into the other. The peaks and dips are caused by irregularities of the fluid interface as a consequence of the random initial particle positioning. As the perturbations grow over time they result in the formation of large-scale RTIs with different wavelengths. We find a similar behavior in our close-to-continuum SMRTI simulation

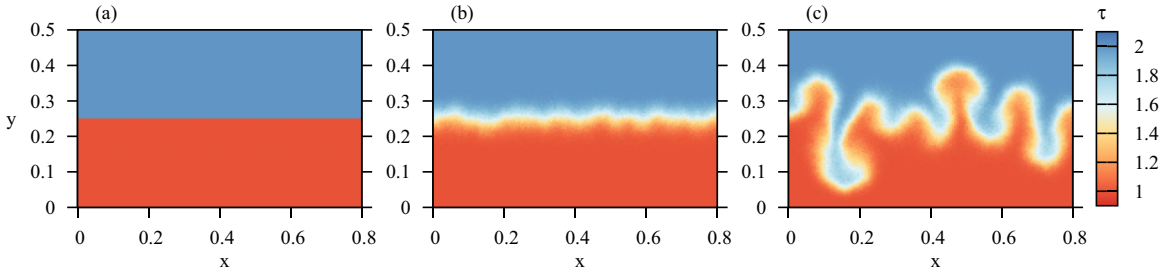

FIG. 2. (Color online) Evolution of fluid instabilities at an initially unperturbed interface of a high-density (blue, above the white separation interface) and a low-density (red, below the white separation interface) fluid in the presence of a gravitational acceleration. The particle number is $N = 10^7$. We plot the particle type τ at times (a) $t = 0$, (b) $t = 1.0$, and (c) $t = 3.0$.

that we discuss in the next section. It is important to point out that a small modification of the particle initialization via, e.g., changed particle positions, can result in a different RTI evolution at later times.

B. The SMRTI close to the continuum limit

We start with a SMRTI simulation close to the hydrodynamic limit by setting $l = l_{\min,1} = 0.025\Delta x$. The box dimensions are $L_x = 0.25$ and $L_y = 1.6$ with 800×5120 calculation bins and 100×640 output bins. The width of a calculation bin is thereby $\Delta x = 3.125\times10^{-4}$. We use $N = 4.0\times10^7$ test particles.

Figure 3 shows the initial particle type τ [Fig. 3(a)], normalized particle number with $N_0 = N/(L_x\times L_y) = 625$ [Fig. 3(b)], and pressure P [Fig. 3(c)]. All quantities are given as averages per output bin and we mirror the results at $x = 0$. Figure 4 provides an estimate on the level of statistical noise in the simulation via y profiles of the density, pressure, and particle type taken at $x = 0.125$. We see significant fluctuations in $N_{\rm bin}$ and P and, as a consequence, will average output quantities over several output bins in our later analysis. The simulation evolves up to $t = 3.75$ and the results for τ are plotted in Fig. 5 for $t = 0.5$ [Fig. 5(a1)], $t = 1.25$ [Fig. 5(a2)], $t = 1.75$ [Fig. 5(a3)], $t = 2.5$ [Fig. 5(a4)], and $t = 3.75$ [Fig. 5(a5)]. For $t \leqslant 1.75$ we add the analytic solution from linear theory using $l = l_{\min,1}$ and $l = l_{\min,2}$ as dashed and solid lines, respectively. For better visualization, the output is limited to $0.2 \leqslant y \leqslant 1.4$.

As before, we see the formation of a diffusion layer for $t \leqslant 0.5$ caused by the finite number of test particles and the finite value of l. At $t = 0.5$, the SMRTI amplitude is in good agreement with the analytic prediction, but small perturbations are present and serve as sources for fluid instabilities that become visible at $t \sim 1.25$. Here, in addition to the growth of the SMRTI, small bubbles of light fluid are visible. Overall, the analytic prediction with $l_{\min,1}$ and $l_{\min,2}$ matches the envelope of the bubble maxima. However, at $t \geqslant 1.75$, the amplitude of the SMRTI significantly lags behind the prediction with $l_{\min,1}$, while $l_{\min,2}$ provides a better fit. The disagreement with $l_{\min,1}$ might indicate that the minimal mean free path is indeed given by $l_{\min,2}$. The SMRTI evolution could also be affected by the secondary instabilities. These are clearly seen for $t \geqslant 1.75$ and might make comparisons with analytic predictions less reliable. Furthermore, a finite mean free path introduces compressibility effects that have been shown to change the

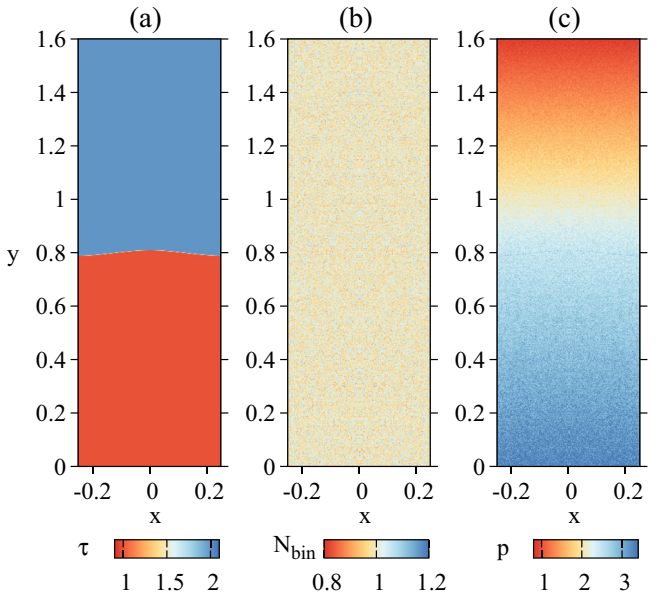

FIG. 3. (Color online) Initialization of SMRTIs with (a) average particle type τ, (b) average particle number $N_{\rm bin}$ in units of $N_0 = 625$, and (c) average pressure p.

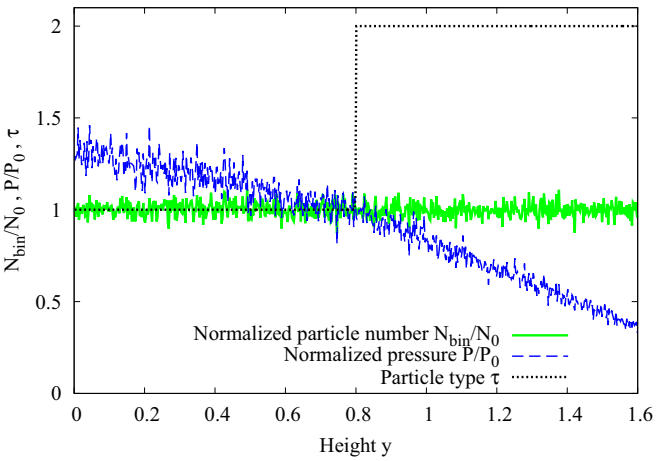

FIG. 4. (Color online) Profiles of the initial average particle density $N_{\rm bin}/N_0$, average particle pressure P/P_0, and particle type τ taken at $x = 0.125$.

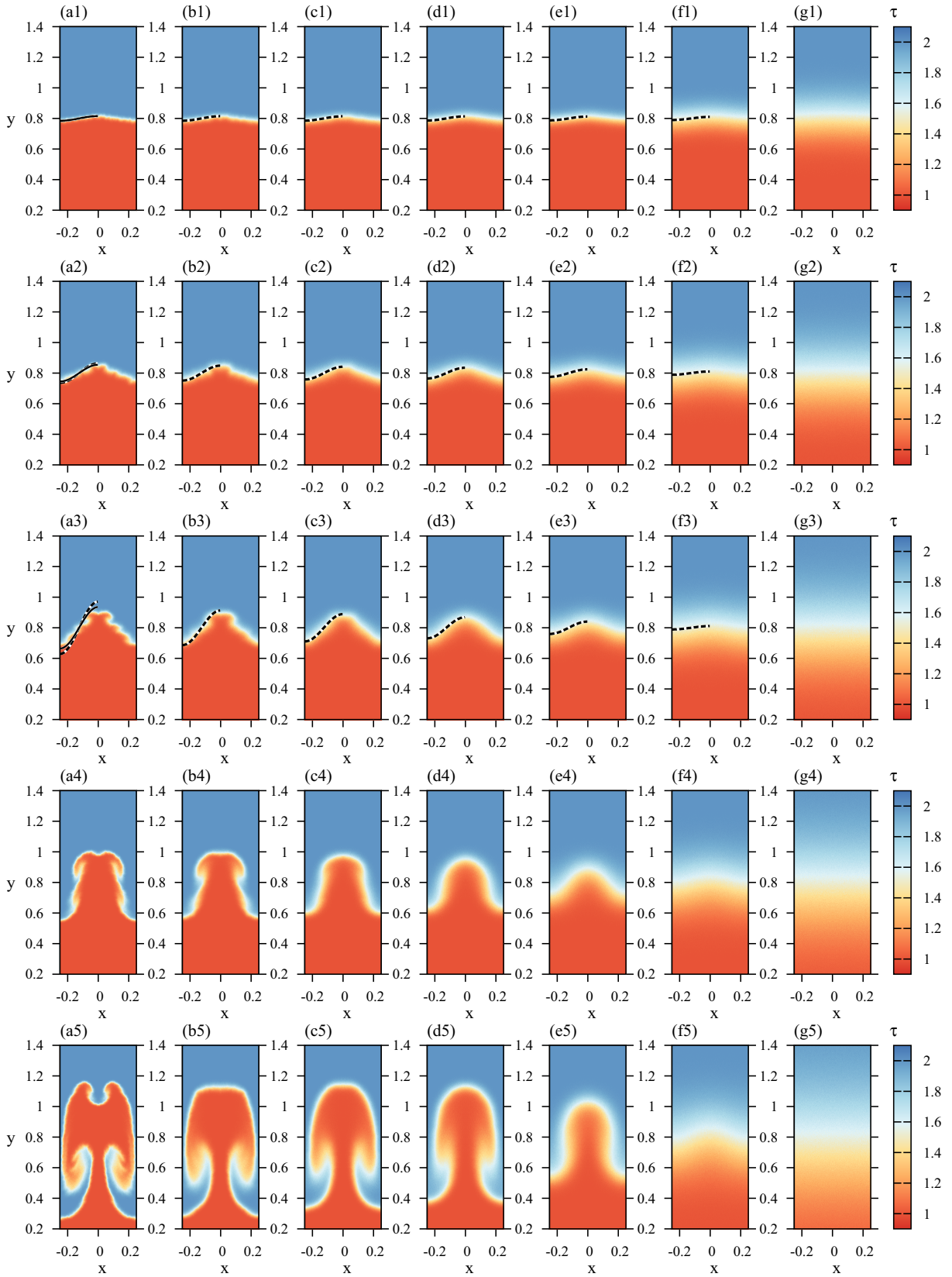

FIG. 5. (Color online) Time evolution of the average particle type τ per bin in the SMRTI simulation for (a) $l = 0.025\Delta x$, (b) $l = 1.5\Delta x$, (c) $l = 3.0\Delta x$, (d) $l = 5.0\Delta x$, (e) $l = 10.0\Delta x$, (f) $l = 30.0\Delta x$, and (g) $l = 100.0\Delta x$. Snapshots are taken at times (1) $t = 0.5$, (2) $t = 1.25$, (3) $t = 1.75$, (4) $t = 2.5$, and (5) $t = 3.75$. Dashed lines give the analytic predictions using the corresponding growth rates for l from Table I. The solid lines in (a1)–(a5) are the analytic solution for $l = l_{\min,2} = 0.56\Delta x$. The number of test particles is $N = 4.0\times10^7$ with 800×5120 simulation bins covering a space of 0.25×1.6.

RTI evolution [71]. To estimate their impact, we calculate the Mach number [85]

$$M = \sqrt{(\rho_1 + \rho_2) g \lambda / 2 P_0}. \tag{45}$$

Our simulations have $M \sim 0.55$ and are therefore in the compressible subsonic flow regime (with $M \lesssim 0.3$ for incompressible subsonic flow). Nonviscous, ideal fluids have a growth rate of $\gamma_i \sim 2.046$ resulting in $\Gamma_i = 17.960$ for $t = 1.75$. When compressibility is included, γ decreases to $\gamma_c \sim 2.01$ [we use Eq. (31) of [75]] and the corresponding amplitude gain is $\Gamma_c(t = 1.75) = 16.865$. The difference between Γ_i and Γ_c is small and the amplitude reduction $\Delta\eta$ for $x = 0$ and $t = 1.75$ is

$$\begin{aligned} \Delta\eta(0,1.75) &= \eta_i(0,1.75) - \eta_c(0,1.75) \\ &\sim 0.980 - 0.969 = 0.011. \end{aligned} \tag{46}$$

This is only about 1.1% of the SMRTI amplitude and thereby too small to account for the disagreement seen in Fig. 5(a3). Of course, the impact of compressibility could be larger when viscosity and diffusion are taken into account. We will return to this point in the next section.

C. Mean-free-path comparison

Figures 5(b)–5(g) show the SMRTI for $l = 1.5\Delta x$ [Fig. 5(b)], $l = 3.0\Delta x$ [Fig. 5(c)], $l = 5.0\Delta x$ [Fig. 5(d)], $l = 10.0\Delta x$ [Fig. 5(e)], $l = 30.0\Delta x$ [Fig. 5(f)], and $l = 100.0\Delta x$ [Fig. 5(g)], whereas (1)–(5) correspond again to different time snapshots as described in the previous section. The jump from $l = 0.025\Delta x$ to $l = 1.5\Delta x$ is motivated by a previous finding that shock wave dynamics do not differ significantly for $l \lesssim \Delta x$ [39]. We expect a similar outcome for the SMRTI simulation. Of course, l still impacts particle diffusion, compressibility, and viscosity [71], however, we expect stronger effects for $l > \Delta x$. For comparison with the simulations, we use again the viscous diffusive growth rates $\Gamma(t)$ from Table I and plot the analytical predictions for $t \leqslant 1.75$ in Fig. 5. It can be seen that the latter agree with the simulations. One possible explanation for the lag of the SMRTI with $l = 0.025\Delta x$ at $t = 1.75$ was the effect of finite compressibility. However, the general agreement between theory and simulations for $1.5\Delta x \leqslant l \leqslant 5\Delta x$ indicates that compressibility does not play a large role for the SMRTI height. The lag therefore is either caused by secondary instabilities or indicates that the true minimal mean free path is given by $l_{\mathrm{min},2}$.

Figure 5 also demonstrates the growth of the mixed fluid layer thickness with l as well as the accompanying blurring of small-scale perturbations. While the simulation with $l = 30.0\Delta x$ still exhibits signs of a weak SMRTI development, no Rayleigh-Taylor evolution can be seen for $l = 100.0\Delta x$ and both fluids simply mix over time as was discussed in Sec. IV B. For such large values of the mean free path, the simulation approaches to the regime of noninteracting gas.

For small l, the average position of the mixing region matches the analytic prediction for $t \lesssim 1.75$. We can also see the impact of the mean free path on the SMRTI amplitude in Figs. 5(a3)–5(g3), where the latter clearly decreases with larger l. For a more quantitative analysis, we plot the amplitude B as a function of time $t \leqslant 1.75$ and scaled time $t_s = t\sqrt{Ag/\lambda}$

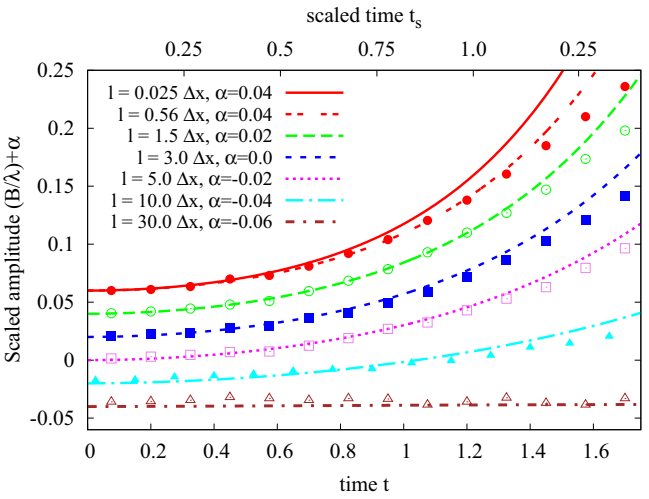

FIG. 6. (Color online) Time evolution of the SMRTI amplitude B for $l = 0.025\Delta x$ (red closed circles), $l = 1.5\Delta x$ (green open circles), $l = 3.0\Delta x$ (blue closed squares), $l = 5.0\Delta x$ (pink open squares), $l = 10.0\Delta x$ (cyan closed triangles), and $l = 30.0\Delta x$ (brown open triangles) scaled by the perturbation wavelength λ together with the linear theory solution (lines).

in Fig. 6. Here B is extracted in the following way: Data are taken from the simulation every $\Delta t = 0.25$ resulting in 75 output files. For each time snapshot, we find the highest point B_{max} for $0.005 \leqslant x \leqslant 0.125$ and $\tau \leqslant 1.8$. Once B_{max} is determined, we pick the lowest point B_{min} with the same x coordinate as B_{max} but $\tau > 1.2$. The height of the SMRTI is then given by the average

$$B = 0.5(B_{\mathrm{max}} + B_{\mathrm{min}}) - 0.8. \tag{47}$$

Furthermore, to suppress statistical noise, we average B over five consecutive snapshots and scale it with λ. The simulation data are plotted as points, while the linear theory predictions are represented by lines. To better distinguish between the different curves, we shift the data sets by a factor α along the y axis. Although the simulation data scatters around the analytic solutions, both generally fit very well at early times. At larger t, especially for $l = 0.025\Delta x$, the instability amplitude increases slower than the analytic prediction with $l = l_{\mathrm{min},1}$, while a better fit is again achieved for $l = l_{\mathrm{min},2}$.

Next we compare the thickness of the diffusion layer, which is determined by

$$D = (B_{\mathrm{max}} - B_{\mathrm{min}}). \tag{48}$$

For the output in Fig. 7, we scale again by λ and see an increase of D with l. Furthermore, we find that $D > B$ for early times, which implies the domination of diffusion over SMRTI growth. The black circles in Fig. 7 mark the times when the latter takes over. While up to this point the width of the mixed fluid layer increases, its growth saturates and even decreases for larger t. This can be caused by displacement of heavy fluid at the top of the light fluid bubble due to its upward motion. Alternatively, the bubble might squeeze matter in the mixed fluid layer due to finite compressibility. Since the decrease is more pronounced for larger l, a cause involving finite matter compressibility seems to be more likely.

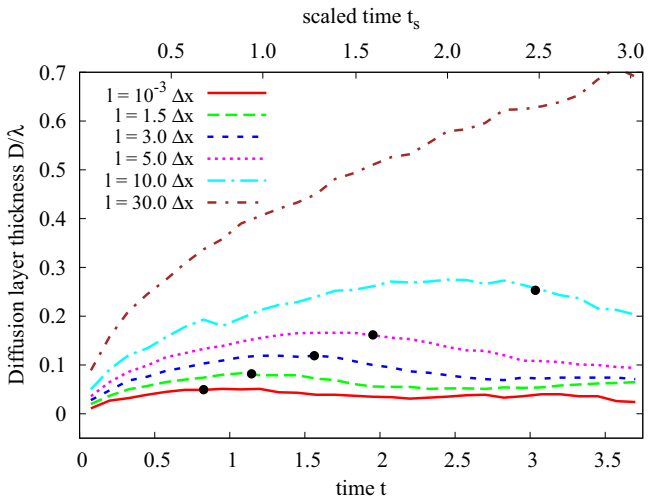

FIG. 7. (Color online) Diffusion layer widths of SMRTI simulations scaled by the perturbation wavelength λ as a function of time. Black circles correspond to points when $B > D$.

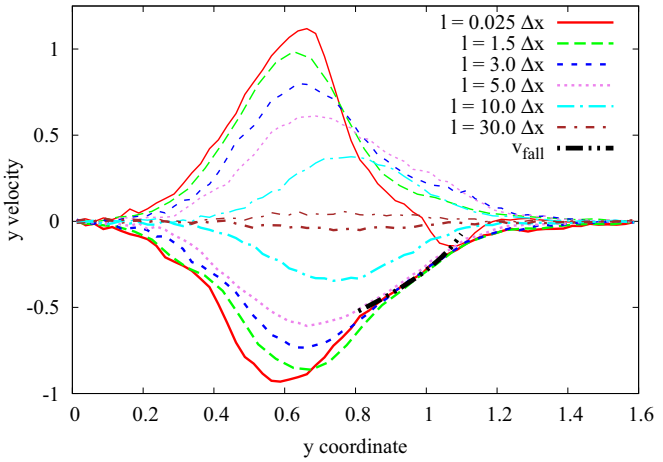

FIG. 9. (Color online) Velocity profiles of the rising SMRTI bubble (thin lines) and sinking spike (thick lines) for different mean free paths l along the y axis at $t = 3.5$. The velocities of the sinking material are compared to the free-fall velocity [74] (thick dash–double-dotted line).

D. Final-state comparison

We now analyze the SMRTI states at $t = 3.75$ and compare them with theoretical predictions. First, we plot the normalized particle density

$$\rho = m_{1,2}n/m_1N_0, \quad m_1 = 10^{-8}, \quad m_2 = 2m_1 \tag{49}$$

in Figs. 8(a)–8(g) as in Fig. 5. We can see two interesting phenomena. First, with larger l, particle densities at the top of the simulation box decrease over time. The effect is visible for $l = 30.0\Delta x$ and $l = 100.0\Delta x$ and is caused by the absence of scattering. Initially, particle velocities are set up according to MB distributions. Over time, the gravitational acceleration increases components in the negative-y direction. Due to the absence of particle interaction, the latter cannot transfer vertical velocity components into other directions and, as a consequence, particles are accelerated downward. Since the absolute particle velocity decrease with height, the effect is most pronounced at the top of the simulation box. The second effect is present for $l \leqslant 3.0\Delta x$ where the density of the heavy fluid at the foot of the SMRTI is increased in comparison to the top of the simulation space. This could be attributed to compressibility as descending spikes squeeze matter when they move downward. Different from the diffusion layer width, the effect is most pronounced for small mean free paths. It could be caused by larger spike velocities for small l, which result in stronger matter compression.

To test this assumption, we determine vertical velocity profiles of the rising bubble and the sinking spike. These are shown in Fig. 9, where we plot the y velocities per bin averaged over $0.005 \leqslant x \leqslant 0.015$ for the rising bubble and $0.235 \leqslant x \leqslant 0.245$ for the descending spike. Furthermore, we average the obtained velocities over ten consecutive output bins in the y direction. The resulting profile shapes generally agree with expectations [74], whereas we find a clear dependence on l. The negative bubble velocity for $l = 0.025\Delta x$ at $1.0 \leqslant y \leqslant 1.2$ is caused by the secondary instability at its top. The largest absolute velocities are found in the $l = 0.025\Delta x$ case, which supports our assumption that

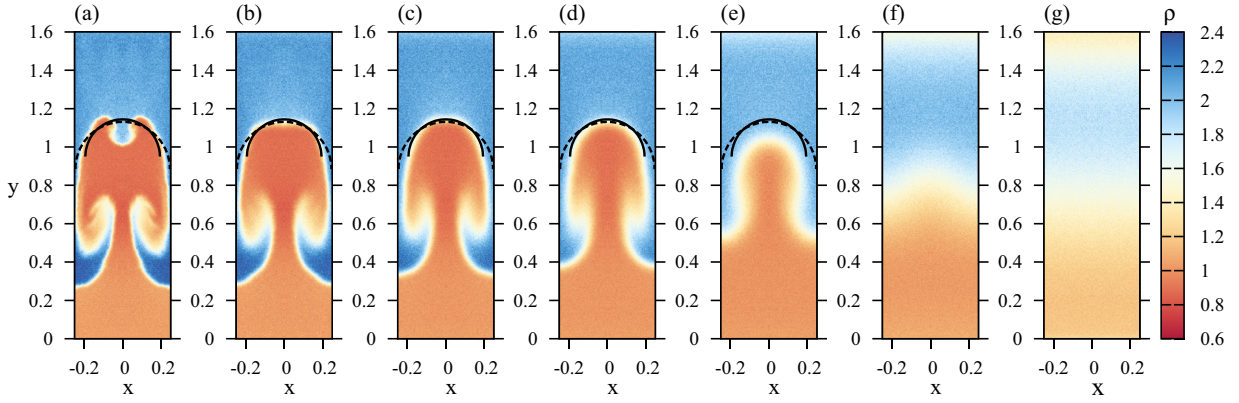

FIG. 8. (Color online) Normalized particle density ρ via Eq. (49) for SMRTI simulations at $t = 3.75$ and different mean free paths l [(a)–(g)] as in Figs. 5(a5)–5(g5). Solid and dashed lines correspond to theoretical estimates for the bubble radius with $R_a = 0.194$ (solid line) and $R = 0.258$ (dashed line) in Eqs. (53) and (54), respectively. See the text for discussion.

the stronger compression of matter occurs due to larger spike velocities for small mean free paths. Starting at the apex of the light fluid bubble, the horizontal component of the spike velocity should be small and the particle motion dominated by the vertical downward component [74]. As a consequence, we can compare the spike velocities to the free-fall velocity of the heavy fluid in the gravitational field [74]

$$v_{\text{fall}}(y) = -\sqrt{2g[1-(\rho_1/\rho_2)](y_b - y)} + v_F,$$
$$v_F = 0.59\sqrt{g[1-(\rho_1/\rho_2)]/k}, \tag{50}$$

where $y_b = 1.132$ marks the average height of the bubble apex for $l \leqslant 5.0\Delta x$. We find that the spike velocities in simulations with $l \leqslant 5.0\Delta x$ agree with $v_{\text{fall}}(y)$ for $0.8 \lesssim y \lesssim 1.1$. The deviations from Eq. (50) in the lower spike region are most likely caused by the influence of the mushroom shape. For larger mean free paths, the velocity profiles become less pronounced. This is due to the larger viscosity and broader spike regions, which allow particles to move horizontally in addition to their vertical motion.

In addition, we can also determine the bubble velocity and compare it with theoretical predictions for its asymptotic value at $t \to \infty$ [86]:

$$v_{\text{bubble},a} = 1.025\sqrt{\frac{2A}{A+1}\frac{g}{3k}}, \tag{51}$$

which implies

$$v_{\text{bubble},a}/\sqrt{g/k} \sim 0.41, \tag{52}$$

whereas [74] gives $v_{\text{bubble},b}/\sqrt{g/k} \sim 0.59$ (interestingly, the two expressions differ by a factor of $\sqrt{2}$). To extract v_{bubble} in our simulations, we average all y velocities per bin in the range $B_{\min} \leqslant y \leqslant B_{\max}$. The latter are determined for $0.005 \leqslant x \leqslant 0.015$. To further reduce statistical noise, we average v_{bubble} over five consecutive time snapshots. Figure 10 shows the simulation results for v_o together with the asymptotic predictions for $v_{\text{bubble},a}$ and $v_{\text{bubble},b}$. For $l = 10\Delta x$ and $l = 30\Delta x$, the bubble velocity rises very slowly. While it eventually reaches $v_{\text{bubble},a}$ for $l = 10\Delta x$, it stays small for $l = 30\Delta x$ due to the large particle diffusion. For $l \leqslant 5\Delta x$, we initially see a linear increase of v_{bubble} with time. The velocities eventually reach a maximum in the range $v_{\text{bubble},a} < v_{\text{bubble}} < v_{\text{bubble},b}$ with a subsequent drop. The latter is more pronounced for smaller mean free paths and, for $l = 0.025\Delta x$, is most likely caused by the secondary instability forming at the top of the bubble [see Fig. 5(a4)]. For $l = 1.5\Delta x$ and $3.0\Delta x$ we find a similar stagnation of v_{bubble}. Although here a secondary instability is not directly visible, the flat bubble top in Figs. 5(b5) and 5(c5) could be interpreted as its onset that decreases v_{bubble}. The effect is very weak for $l = 5.0\Delta x$. Here the top of the bubble is round and the velocity does not exhibit a large decrease with time.

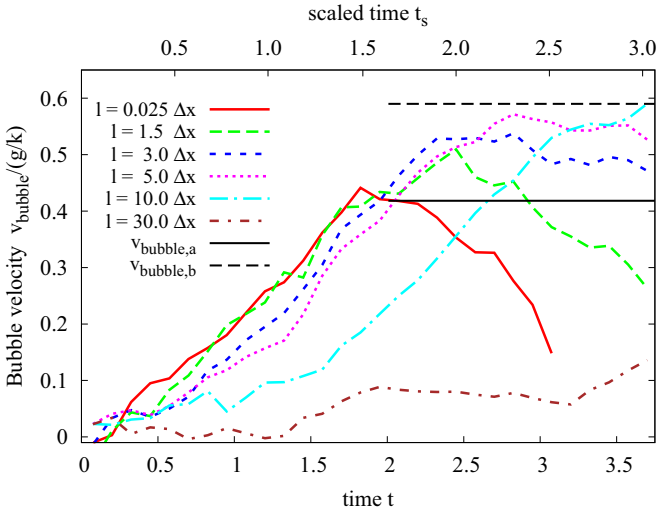

FIG. 10. (Color online) Scaled velocity of the SMRTI bubble as a function of time for different mean free paths l. The horizontal solid and dashed lines are theoretical estimates of the asymptotic bubble velocity [74,86] (see the text).

Another effect that needs to be addressed in the future is the size of the simulation space. As the light fluid bubble rises, it approaches the upper boundary of the simulation space. Although we apply random reflective boundary conditions, wave reflection might still occur and, when propagating downward, could interact with the bubble and cause it to deform or decelerate. In addition, as the bubble rises and expands, it comes very close to the vertical box boundaries. These can impact the evolution of the SMRTI by preventing its full expansion. To explore the latter, we compare the radius of the light fluid bubble with theoretical predictions. The 2D asymptotic value of the bubble curvature κ was determined in [86] for an ideal fluid to be

$$\kappa_a = -2\pi/4.88\lambda \sim -2.575, \tag{53}$$

with a corresponding radius $R_a = -1/2\kappa_2 \sim 0.194$, and in [87] (using Fig. 1 of the reference with $\zeta_1/k \sim -0.105$) to be

$$\kappa_b \sim -0.105(16\pi/3\sqrt{3}\lambda) \sim -2.031. \tag{54}$$

The latter results in $R_b \sim 0.246$. It is noteworthy that $R_b \sim L_x$, which might lead to wall effects in the late stages of the SMRTI. We plot semicircles with R_a (solid line) and R_b (dashed line) together with the particle densities of the SMRTIs in Fig. 8. Since R_a and R_b are derived for ideal fluids, we expect the best fit for close-to-continuum simulations, while both radii should overestimate the bubble size for calculations with large mean free paths. This effect is clearly seen for $l = 10.0\Delta x$. However, R_a seems to reproduce the SMRTI with $l \sim 5.0\Delta x$ best, while underestimating the bubble for smaller mean free paths. This could imply that R_b is a better estimate of the radius, however, when comparing with numerical results we find that R_b seems to always overestimate the SMRTI bubble, even for $l = 0.025\Delta x$. This could be due to the small width of the simulation space, which might restrict the bubble and result in a smaller radius. Studies of the SMRTI in a bigger simulation space need to address the bubble evolution in the future.

E. The SMRTI with small mean free paths

As mentioned before, the particle mean free path in our studies is limited by a minimal value $l_{\min}$. Considering that collision partners cannot be farther away than $\sim 2\Delta x$, this value should be given by $l_{\min,1} = 0.025\Delta x$. On the other hand, when assuming that for large N_{bin} collision partners are typically close to each other and using an average distance

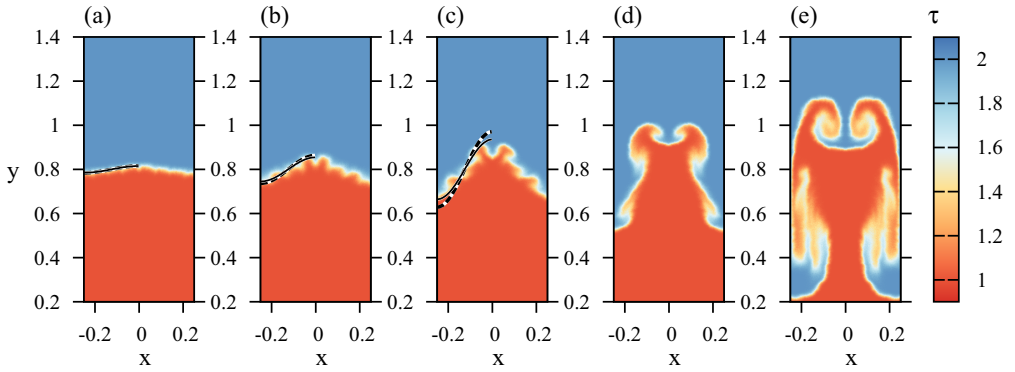

FIG. 11. (Color online) Particle type τ for the SMRTI with diffusion suppression, mean free path $l = 10^{-3}\Delta x$, and particle number $N = 4.0\times10^7$. (a)–(e) correspond to different simulation times as in Fig. 5. Dashed lines give the analytic prediction for the SMRTI amplitude for $l = l_{\mathrm{min},1} = 0.025\Delta x$, while solid lines were obtained using $l = l_{\mathrm{min},2} = 0.56\Delta x$.

of $2\sqrt{A_{\mathrm{bin}}/\pi N_{\mathrm{bin}}}$, the minimal mean free path increases to $l_{\mathrm{min},2} \sim 0.56\Delta x$ (see the discussion in Sec. IV D). Previously, we argued that simulations should evolve similarly for $l \leqslant l_{\mathrm{min}}$, especially properties such as diffusion layer width and SMRTI amplitude, quantities that directly depend on l, should not differ much. We will test this assumption by setting $l \ll \Delta x = 10^{-3}\Delta x$ and performing a SMRTI simulation.

Figure 11 shows the corresponding simulation snapshots with Figs. 11(a)–11(g) as in Fig. 5. While the diffusion layer width is very similar to $l = 0.025\Delta x$, large-wave-number instabilities seem to be more pronounced. This is clearly visible in Figs. 11(b) and 11(c). Furthermore, in the latter, the upper small-scale instability develops into a RTI itself. The corresponding small fluid bubble moves upward together with the SMRTI. As it approaches the simulation walls, the lower part of the bubble is deflected downward while the upper part continues to move upward, distorting the mushroom shape.

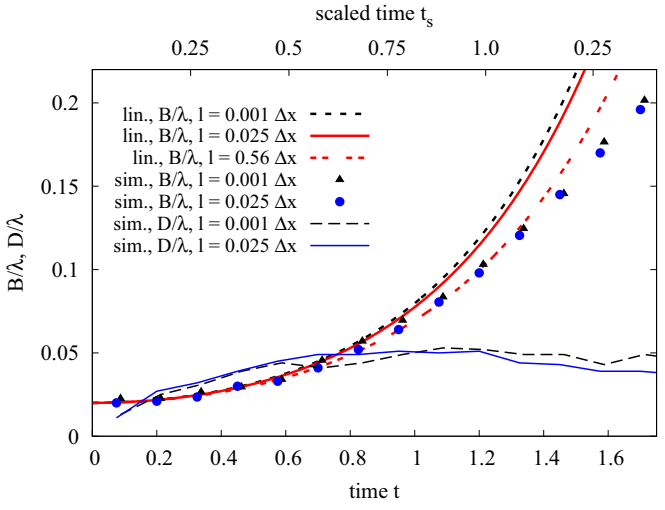

FIG. 12. (Color online) Scaled amplitude B/λ (closed triangles and circles) for $l = 10^{-3}\Delta x$ and $l = 0.025\Delta x$ together with the linear theory predictions (thick lines) for $l = 10^{-3}\Delta x$, $l = 0.025\Delta x$, and $l = 0.56\Delta x$. Simulation results for the diffusion layer width D/λ for $l = 10^{-3}\Delta x$ and $l = 0.025\Delta x$ are given by thin dashed and solid lines, respectively.

For a quantitative comparison of the SMRTI amplitude and diffusion layer width, we determine both as in Sec. V C and plot them together with the simulation result for $l = 0.025\Delta x$ and linear theory predictions for $l = 10^{-3}\Delta x$, $l = 0.025\Delta x$, and $l = 0.56\Delta x$ in Fig. 12. The formation of secondary instabilities for $l = 10^{-3}\Delta x$ complicates a reliable determination of the SMRTI amplitude and, as a consequence, we limit the comparison to $t \leqslant 1.75$. As we can see, the linear theory solution predicts a slightly higher amplitude for $l = 10^{-3}\Delta x$ in comparison to $l = 0.025\Delta x$. The values for B/λ in the simulations, on the other hand, are very similar. The same applies to the diffusion layer widths. This confirms our prediction that mean-free-path dependent quantities, such as SMRTI amplitude and mixed layer width, are given by the true minimal value of l_{min}. The more pronounced small-scale structures for $l = 10^{-3}\Delta x$ might be caused by a different sequence of random numbers in the simulation. For close-to-continuum simulations, small differences at early times could lead to different perturbations of the fluid interface and result in different SMRTI evolutions.

VI. SUMMARY AND OUTLOOK

We presented simulations of single-mode Rayleigh-Taylor instabilities with a large-scale modified direct simulation Monte Carlo code. Our approach combines the computational scaling of DSMC methods and the spatial accuracy of the point-of-closest-approach technique. The aim of the current work was to test our kinetic code on its ability to reproduce fluid instabilities and study the latter for finite viscosity and diffusion. The code has been validated in the hydrodynamic regime by 2D and 3D shock wave studies in the past and is able to simulate matter for a large range of Knudsen numbers. For our RTI simulations, we applied $N = 4.0\times10^7$ test particles. At early stages of the SMRTI, the growth rate can be analytically obtained from linear theory while for late times the onset of secondary instabilities and turbulent mixing is seen by hydrodynamic codes and experiments. We compared our simulations to the expected behavior of the SMRTI in these regimes. Our kinetic method is limited by a minimal value for the particle mean free path l, which depends on the particle number per simulation cell. By applying different l we were able to simulate matter in a regime that is close

to the continuum limit and for nonequilibrium matter. For $l \lesssim 5\Delta x$, we found the characteristic mushroom shape of the SMRTI, which was observed in hydrodynamic simulations and experiments. Furthermore, in our close-to-continuum simulations, initial irregularities of the fluid interface result in the formation of large-wave-number instabilities that evolve into RTIs themselves. A diffusion layer, caused by particles moving from one fluid into the other, is always present. Its width increases for larger l while small-scale structures become blurred. For large mean free paths, simulations eventually approach the regime of noninteracting gas.

Overall, our simulations agree with the analytic prediction from linear theory including diffusion and viscosity and lead to similar SMRTI shapes as we would expect from hydrodynamic studies. We conclude that our kinetic approach can reproduce the general features of SMRTI. In the future, we plan to perform convergence tests with a larger number of test particles and thereby smaller mean free paths as well as more general fluid instability studies. With that, together with the already successfully passed shock wave tests, we will be able to direct our attention to the simulation of, e.g., astrophysical systems, such as core-collapse supernovas.

ACKNOWLEDGMENTS

This work used the Extreme Science and Engineering Discovery Environment, which is supported by National Science Foundation Grant No. OCI-1053575. Furthermore, I.S. acknowledges the support of the High Performance Computer Center and the Institute for Cyber-Enabled Research at Michigan State University. This research was supported in part by Lilly Endowment, Inc., through its support for the Indiana University Pervasive Technology Institute, and in part by the Indiana METACyt Initiative. The Indiana METACyt Initiative at Indiana University is also supported in part by Lilly Endowment, Inc. Furthermore, the authors would like to thank LANL physicists Daniel Livescu and Wesley Even for useful discussions.

[1] P. K. Schelling, S. R. Phillpot, and P. Keblinski, Phys. Rev. B **65**, 144306 (2002).
[2] K. Kadau, T. C. Germann, P. S. Lomdahl, and B. L. Holian, Science **296**, 1681 (2002).
[3] W. Bauer, G. F. Bertsch, W. Cassing, and U. Mosel, Phys. Rev. C **34**, 2127 (1986).
[4] G. F. Bertsch, H. Kruse, and S. Das Gupta, Phys. Rev. C **29**, 673(R) (1984).
[5] H. Kruse, B. V. Jacak, and H. Stöcker, Phys. Rev. Lett. **54**, 289 (1985).
[6] J. Aichelin and G. Bertsch, Phys. Rev. C **31**, 1730 (1985).
[7] J. Aichelin and H. Stöcker, Phys. Lett. B **176**, 14 (1986).
[8] I. Bouras, A. El, O. Fochler, H. Niemi, Z. Xu, and C. Greiner, Phys. Lett. B **710**, 641 (2012).
[9] G. Kortemeyer, W. Bauer, K. Haglin, J. Murray, and S. Pratt, Phys. Rev. C **52**, 2714 (1995).
[10] M. Casanova, O. Larroche, and J.-P. Matte, Phys. Rev. Lett. **67**, 2143 (1991).
[11] F. Vidal, J. P. Matte, M. Casanova, and O. Larroche, Phys. Fluids B: Plasma Phys. **5**, 3182 (1993).
[12] F. Vidal, J. P. Matte, M. Casanova, and O. Larroche, Phys. Rev. E **52**, 4568 (1995).
[13] N. Roth and D. Kasen, Astrophys. J. Suppl. Ser. **217**, 9 (2015).
[14] R. T. Wollaeger, D. R. van Rossum, C. Graziani, S. M. Couch, G. C. Jordan IV, D. Q. Lamb, and G. A. Moses, Astrophys. J. Suppl. **209**, 36 (2013).
[15] J. D. Densmore and E. W. Larsen, J. Comput. Phys. **199**, 175 (2004).
[16] N. A. Gentile, J. Comput. Phys. **172**, 543 (2001).
[17] L. B. Lucy, Astron. Astrophys. **345**, 211 (1999).
[18] J. A. Fleck Jr. and E. H. Canfield, J. Comput. Phys. **54**, 508 (1984).
[19] J. A. Fleck Jr. and J. D. Cummings, J. Comput. Phys. **8**, 313 (1971).
[20] L. Hernquist and J. P. Ostriker, Astrophys. J. **386**, 375 (1992).
[21] A. S. Schneider, C. J. Horowitz, J. Hughto, and D. K. Berry, Phys. Rev. C **88**, 065807 (2013).
[22] E. Abdikamalov, A. Burrows, C. D. Ott, F. Löffler, E. O'Connor, J. C. Dolence, and E. Schnetter, Astrophys. J. **755**, 111 (2012).
[23] H.-T. Janka and W. Hillebrandt, Astron. Astrophys. Suppl. Ser. **78**, 375 (1989).
[24] J. Lindl, Phys. Plasmas **2**, 3933 (1995).
[25] J. D. Lindl, P. Amendt, R. L. Berger, S. G. Glendinning, S. H. Glenzer, S. W. Haan, R. L. Kauffman, O. L. Landen, and L. J. Suter, Phys. Plasmas **11**, 339 (2004).
[26] S. H. Glenzer, D. A. Callahan, A. J. MacKinnon, J. L. Kline, G. Grim, E. T. Alger, R. L. Berger, L. A. Bernstein, R. Betti, Bleuel *et al.*, Phys. Plasmas **19**, 056318 (2012).
[27] M. J. Edwards, P. K. Patel, J. D. Lindl, L. J. Atherton, S. H. Glenzer, S. W. Haan, J. D. Kilkenny, O. L. Landen, E. I. Moses, A. Nikroo *et al.*, Phys. Plasmas **20**, 070501 (2013).
[28] K. Kadau, T. C. Germann, and P. S. Lomdahl, Int. J. Mod. Phys. C **17**, 1755 (2006).
[29] T. A. Brunner and P. S. Brantley, J. Comput. Phys. **228**, 3882 (2009).
[30] P. Jonsson and J. R. Primack, New Astron. **15**, 509 (2010).
[31] F. Ercolessi, "A molecular dynamics primer", Spring College in Computational Physics, ICTP, Trieste (1997).
[32] D. Frenkel and B. Smit, *Understanding Molecular Simulation*, 2nd ed. (Academic Press, Orlando, FL, 2001).
[33] G. A. Bird, Phys. Fluids **6**, 1518 (1963).
[34] G. A. Bird, *Molecular Gas Dynamics and the Direct Simulation of Gas Flows* (Clarendon Press, Oxford, 1994).
[35] G. A. Bird, in *Rarefied Gas Dynamics*, edited by J. H. de Leeuw (Academic Press, New York, 1965), Vol. 1, p. 216.
[36] D. Tskhakaya, in *Computational Many Particle Physics*, edited by H. Fehske, R. Schneider, and A. Weie, Lecture Notes in Physics (Springer, Berlin, Heidelberg, 2008), Vol. 739, pp. 161–189.
[37] R. W. Hockney and J. W. Eastwood, *Computer Simulation Using Particles* (Taylor & Francis, Bristol, PA, 1988).
[38] I. Bouras, E. Molnár, H. Niemi, Z. Xu, A. El, O. Fochler, C. Greiner, and D. H. Rischke, Phys. Rev. Lett. **103**, 032301 (2009).
[39] I. Sagert, W. Bauer, D. Colbry, J. Howell, R. Pickett, A. Staber, and T. Strother, J. Comput. Phys. **266**, 191 (2014).
[40] Z.-H. Li and H.-X. Zhang, J. Comput. Phys. **193**, 708 (2004).

[41] Y. Gan, A. Xu, G. Zhang, X. Yu, and Y. Li, Physica A: Stat. Mech. Appl. **387**, 1721 (2008).

[42] K. Xu and J.-C. Huang, J. Comput. Phys. **229**, 7747 (2010).

[43] P. Degond, G. Dimarco, and L. Mieussens, J. Comput. Phys. **229**, 4907 (2010).

[44] G. Dimarco and R. Loubere, J. Comput. Phys. **255**, 680 (2013).

[45] K. Kadau, J. L. Barber, T. C. Germann, B. L. Holian, and B. J. Alder, R. Soc. London Philos. Trans. Ser. A **368**, 1547 (2010).

[46] K. Kadau, T. C. Germann, N. G. Hadjiconstantinou, P. S. Lomdahl, G. Dimonte, B. L. Hoian, and B. J. Adler, Proc. Natl. Acad. Sci. USA **101**, 5851 (2004).

[47] J. N. Glosli, D. F. Richards, K. J. Caspersen, R. E. Rudd, J. A. Gunnels, and F. H. Streitz, in *Proceedings of the 2007 ACM/IEEE Conference on Supercomputing, SC '07* (ACM, New York, NY, 2007), pp. 58:1–58:11.

[48] M. D. Weinberg, Mon. Not. R. Astron. Soc. **438**, 2995 (2014).

[49] J. Ashwin and R. Ganesh, Phys. Rev. Lett. **104**, 215003 (2010).

[50] V. V. Zhakhovskii, S. V. Zybin, S. I. Abarzhi, and K. Nishihara, in *Shock Compression of Condensed Matter*, edited by M. D. Furnish, M. Elert, T. P. Russell, and C. T. White, American Institute of Physics Conference Series (AIP Publishing LLC, Melville, 2006), Vol. 845, pp. 433–436.

[51] S. V. Zybin, V. V. Zhakhovskii, E. M. Bringa, S. I. Abarzhi, and B. Remington, AIP Conf. Proc. **845**, 437 (2006).

[52] V. Zhakhovskii, K. Nishihara, and M. Abe, in *Proceedings of the 2nd International Conference on Inertial Fusion Science and Applications, IFSA2001*, edited by K. A. Tanaka, D. D. Meyerhofer, and J. Meyer-ter-Vehn (Elsevier, Paris, 2002), pp. 106–109.

[53] K. Nishihara, J. G. Wouchuk, C. Matsuoka, R. Ishizaki, and V. V. Zhakhovsky, R. Soc. London Philos. Trans. Ser. A **368**, 1769 (2010).

[54] H. A. Bethe, Rev. Mod. Phys. **62**, 801 (1990).

[55] H.-T. Janka, Annu. Rev. Nucl. Part. Sci. **62**, 407 (2012).

[56] S. E. Bodner, Phys. Rev. Lett. **33**, 761 (1974).

[57] M. J. Rosenberg, H. G. Rinderknecht, N. M. Hoffman, P. A. Amendt, S. Atzeni, A. B. Zylstra, C. K. Li, F. H. Séguin, H. Sio, M. G. Johnson *et al.*, Phys. Rev. Lett. **112**, 185001 (2014).

[58] O. A. Hurricane, D. A. Callahan, D. T. Casey, P. M. Celliers, C. Cerjan, E. L. Dewald, T. R. Dittrich, T. Döppner, D. E. Hinkel, L. F. B. Hopkins *et al.*, Nature **506**, 343 (2014).

[59] S. A. Colgate and R. H. White, Astrophys. J. **143**, 626 (1966).

[60] C. D. Ott, E. Abdikamalov, P. Mösta, R. Haas, S. Drasco, E. P. O'Connor, C. Reisswig, C. A. Meakin, and E. Schnetter, Astrophys. J. **768**, 115 (2013).

[61] A. Burrows, Rev. Mod. Phys. **85**, 245 (2013).

[62] K. Sumiyoshi and S. Yamada, Astrophys. J. Suppl. **199**, 17 (2012).

[63] S. W. Bruenn, A. Mezzacappa, W. R. Hix, E. J. Lentz, O. E. Bronson Messer, E. J. Lingerfelt, J. M. Blondin, E. Endeve, P. Marronetti, and K. N. Yakunin, Astrophys. J. Lett. **767**, L6 (2013).

[64] I. Sagert, W. Bauer, D. Colbry, R. Pickett, and T. Strother, J. Phys.: Conf. Ser. **458**, 012031 (2013).

[65] R. Liska and B. Wendroff, in *Hyperbolic Problems: Theory, Numerics, Applications*, edited by T. Y. Hou and E. Tadmor (Springer, Berlin, Heidelberg, 2003), pp. 831–840.

[66] Y. Gan, A. Xu, G. Zhang, and Y. Li, Phys. Rev. E **83**, 056704 (2011).

[67] Rayleigh, Proc. London Math. Soc. **s1-14**, 170 (1882).

[68] G. Taylor, Proc. R. Soc. London Ser. A. Math. Phys. Sci. **201**, 192 (1950).

[69] D. H. Sharp, Phys. D Nonlinear Phenom. **12**, 3 (1984).

[70] H. J. Kull, Phys. Rep. **206**, 197 (1991).

[71] T. Wei and D. Livescu, Phys. Rev. E **86**, 046405 (2012).

[72] S. Chandrasekhar, *Hydrodynamic and Hydromagnetic Instabilities* (Clarendon Press, Oxford, 1961).

[73] E. A. Frieman, Astrophys. J. **120**, 18 (1954).

[74] N. A. Inogamov, Astrophys. Space Phys. Rev. **10**, 1 (1999).

[75] D. Livescu, Phys. Fluids **16**, 118 (2004).

[76] X. Ribeyre, V. T. Tikhonchuk, and S. Bouquet, Phys. Fluids **16**, 4661 (2004).

[77] S. Chapman and T. G. Cowling, in *The Mathematical Theory of Non-Uniform Gases*, 3rd ed. (Cambridge University Press, Cambridge, 1970), p. 47.

[78] T. Strother and W. Bauer, Int. J. Mod. Phys. D **19**, 1483 (2010).

[79] T. Strother and W. Bauer, Int. J. Mod. Phys. E **16**, 1073 (2007).

[80] W. Bauer and T. Strother, Int. J. Mod. Phys. E **14**, 129 (2005).

[81] J. Howell, W. Bauer, D. Colbry, R. Pickett, A. Staber, I. Sagert, and T. Strother, in *Proceedings of Nuclear Physics: Presence and Future*, FIAS Interdisciplinary Science Series (Springer International Publishing, Switzerland, 2014), Vol. 2.

[82] I. Sagert, W. Bauer, D. Colbry, J. Howell, A. Staber, and T. Strother, J. Phys.: Conf. Ser. **535**, 012032 (2014).

[83] J. L. Plawsky, *Transport Phenomena Fundamentals* (CRC Press, Boca Raton, FL, 2014).

[84] R. E. Duff, F. H. Harlow, and C. W. Hirt, Phys. Fluids **5**, 417 (1962).

[85] S. J. Reckinger, D. Livescu, and O. V. Vasilyev, Phys. Scripta **2010**, 014064 (2010).

[86] V. N. Goncharov, Phys. Rev. Lett. **88**, 134502 (2002).

[87] S. I. Abarzhi, K. Nishihara, and J. Glimm, Phys. Lett. A **317**, 470 (2003).